2D in situ X-ray imaging of aluminium foam during deformation

Bjørnar Askeland Flatøe

Department of Physics, NTNU

Sammendrag

Dette studiet ble gjennomført for å bestemme nytteverdien av todimensjonale in situ røntgen avbildninger for å undersøke dynamiske prosesser i tredimensjonale prøver. Aluminium skum ble undersøkt ved bruk av radiogram of computertomografi mens prøven ble utsatt for en serie små kompresjoner. For hvert steg av kompresjonen ble radiogrammene av to ortogonale projeksjoner lagret, mens det ved utvalgte steg også ble gjennomført fullstendige tomogrammer. Det ble i radiogrammene observert deformasjoner, og radiogrammene ble sammenlignet med tomogrammene før og etter deformasjon for undersøke i hvor stor grad de samsvarte. Deformasjonene som ble observert i radiogrammene stemte vel overens med endringer i tomogrammene, men kun enkelte deformasjoner var synlige i et gitt radiogram. En hendelse som var svært enkel å oppdage i en projeksjon gav ingen utslag i den andre projeksjonen som ble brukt. In situ radiogrammer gjorde det mulig å observere enkelte deformasjonshendelser med en mye bedre tidsoppløsning enn det som er mulig for fulle computertomogrammer, men kun for de hendelsene som omhandlet vegger parallelle med projeksjonsretningen.

Abstract

This study was conducted to determine the usefulness of 2D in situ x-ray measurements at the home laboratory to examine the dynamic processes in 3D samples. A sample of aluminium foam was examined by radiograms and computed tomograms as the sample was compressed in small steps. Two perpendicular radiograms were taken at each step while the full tomograms were aquired at some selected steps. The radiograms showed some deformation, and the radiograms were compared to the tomograms before and after the deformation to determine the degree of correlation. The events detected in the radiograms were in accordance with the changes observed in the tomograms, however only certain events were detectable from a single projection. When utilising two projections for the radiograms some deformation events were detected in one, but did not show up in the other radiogram. 2D in situ x-ray imaging was able to show the deformation on a time resolution not possible for full tomograms in the home laboratory, but only for certain events for a given projection direction of the radiogram, namely those events that concerned parallel walls deforming.

Preface

This study was conducted as a master thesis in Physics at the Department of Physics at NTNU. The study was done as a collaboration between the x-ray group at the Department of Physics and The Center for Advanced Structural Analysis, CASA, at NTNU. The goal for the thesis was to examine whether time-resolved 2D x-ray images would provide a beneficial insight into the structural deformation of metal foams using the x-ray machine at the Department of Physics, allowing for in situ measurements of deformation processes without the use of synchrotrons.

I would not have been able to complete this project without the continued support from my supervisor Ragnvald Mathiesen and my co-supervisor Federico Hector Corva who helped point me in the right direction whenever I hit a wall and always ready to guide my efforts in the right direction. I'd also like to thank Arild Holm Clausen and Odd Sture Hoppestad at CASA for their interest which made presenting my results to them so enjoyable. I'd like to thank Sindre at CASA for assisting with the compression rig during the experiment. Finally I'd like to thank the members of the x-ray research group at the Department of Physics, NTNU for community spirit that was ever present, and Ole Tore Buset for quickly getting the x-ray machine up and running again when it needed maintenance in the middle of my experiment.

Contents

1. Introduction

1.1. Motivation

Metal foams are metals that have, though one process or another, been filled with cavities causing the metal to have a lower density. A lower density means that the foam can be compressed by the application of external forces, which could potentially make metal foams ideal shock absorbers.

A technique by which to characterise metal foams are by way of performing a computed tomography (CT) scan of a sample using X-rays. CT allows for reconstruction of the volume in three dimensions on the micrometer scale, and is very useful in determining the interior characteristics of an produced foam. While the macroscopic deformation strength of metal foams have been previously studied[1], there is still a lot to learn about the process on the smaller scale.

To learn more about the strength and malleability of metal foams it is interesting to examine the deformation process in real time to gain additional insight into the small scale responses to the application of external forces. A full resolution CT scan takes a lot of time in the home laboratory, and as such it is desirable to find a

A solution to obtain a time-resolved series of X-ray images has been proposed, which is to collect fewer images, with the consequence that volume reconstruction is no longer possible. By carefully selecting the angles that will be examined, and comparing the final result with the CT scans prior to and after the deformation, the process can be studied in a time resolved manner based on the radiograms, providing valuable insight.

1.2. Earlier studies

In 1998 a study by J. Banhart and J. Baumeister[1] examined the mechanical deformation characteristics of aluminium and zinc foams. A review by J. Banhart[2] on the production of metal foams have also been considered, as it gives insight into the field of manufacturing. A short introduction to the process used to produce the samples in this study will be presented later in this text, while a more complete introduction to this method can be found on pages 574-581 in the review by J. Banhart. The process of determining characteristics in metal foams using X-rays is also briefly discussed in the review.

A feasibility study of the technique was conducted in the autumn of 2018 at the Department of Physics, NTNU. This study focused on whether radiograms could be used to detect changes in density in aluminium foams as a result of compression. Additionally the study served as a firsthand examination of how aluminium foam behaved during compression by using an optical camera set to take surface images of the foam during compression. The camera proved useful in understanding how the foam compressed over time, but as it was an optical camera it was only able to give information on the surface layer of the sample. The camera was hence unable to examine the evolution of an intact pore in the interior of the sample, which is the aim of the 2D in situ x-ray imaging in the study described in

this thesis. The optical camera in the feasibility study did however emphasis the value of a series of in situ images over time. The feasibility study also showed that changes of density in an aluminium foam could be detected by examining the radiograms of the sample. The promising results from this feasibility study formed the basis of the study behind this thesis.

1.3. Material applications

The deformation characteristics of metal foams in regards to compression makes metal foams ideal for applications such as shock absorbers, however they have until recently been too expensive to manufacture or have produced too unpredictable results.

Due to fairly recent developments in the production process the possibility of using metal foam in various applications have increased. As a metal foam is far less dense than a regular metal, the possibility of using it as a lightweight alternative to regular metal in e.g. planes is also an interesting prospect, but this requires a higher understanding of the material. By increasing our understanding of this structure, its suitability for other applications might also become apparent.

1.4. Technique applications

The technique examined in this thesis would allow for in situ x-ray measurements in a home laboratory. If the technique proved useful it could be used to examine the interior of dynamical systems without the use of synchrotrons or similar high-end equipment, greatly improving the possibility of performing in situ experiments requiring x-rays.

2. Theory

2.1. X-Ray generation in home laboratories

In the home laboratory the most common way of generating x-ray beams is with a sealed tube generator, in which accelerated electrons are directed toward a metal target. The x-ray beam generated by sealed tube generators can be considered as the combination of two phenomena, the bremsstrahlung and the characteristic radiation. The bremsstrahlung is released through repeated interactions between the incoming electrons and the Coulomb field of the atoms in the metallic target. The bremsstrahlung forms a continuous spectrum with intensities given by Kramers' law[3]:

$$I_{brems}(E)dE = k_1 \cdot (E_{max} - E) \, EdE. \tag{1}$$

where k_1 is a material specific constant and the maximum energy $E_{max} = eV$, where e is the fundamental charge and V is the acceleration voltage of the tube.

Characteristic X-rays are produced when an incoming electron has an energy that is equal to or larger than the binding energy of a core electron in the target. As the incoming electron transfers energy to the core electron, the core electron is brought into continuum, ionising the metal atom and leaving behind a core hole. An electron in a higher energy state then fills the core hole, and the energy difference between the two levels is released as a photon, see Fig. 1 for an illustration of this process. Since the wavelength produced is a direct result of the energy difference between the two electron states in the metal atom, the energy of the characteristic X-rays produced is determined by the metal used as target.
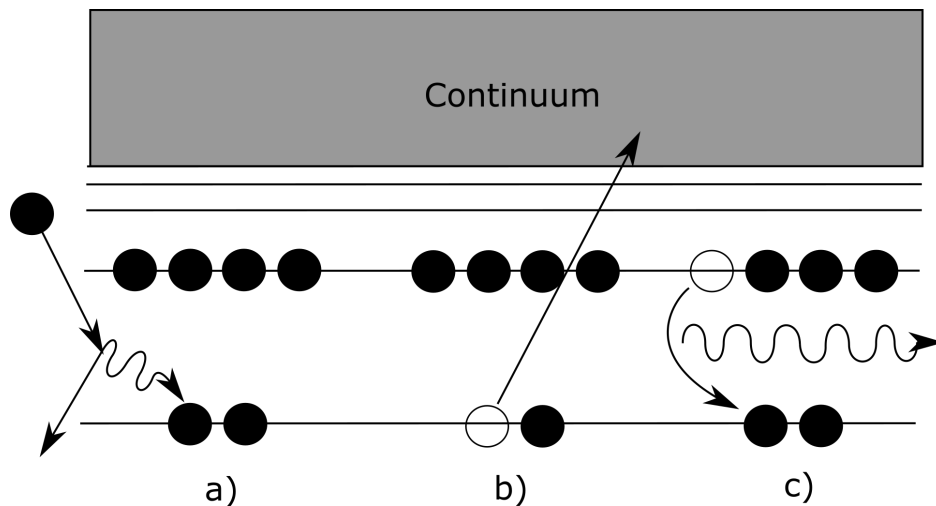

Figure 1: The process by which characteristic X-rays are emitted from a material. a) An incoming high-energy electron transfers some of its energy to a core electron. b) The core electron gain enough energy to be brought into continuum, ionising the parent atom. c) Another electron fills the gap left behind and the excess energy this electron previously contained is released as a photon.

The intensity of each characteristic radiation is given by[4]

3

$$I(E_{char}) = k_2 \cdot i(V - e \cdot E_{char})^{\frac{3}{2}} \tag{2}$$

where i is the operating current of the tube, k_2 is a source-specific constant, V is the acceleration voltage of the tube and E_{char} is the energy required to remove an electron from the target atom. There will be multiple E_{char} for a single atom,

2.2. Transmission and attenuation

An X-ray beam which passes through a material will be attenuated as a result of photon-matter interactions. The likelihood of photon-matter interactions happening is called the cross section of the interaction, σ. The most important photon-matter interactions for conventional x-ray imaging are the photoelectric effect, σ_{pe}, Compton scattering, σ_C, and pair production, σ_{pp}.

The photoelectric effect is the process in which an incoming photon is absorbed by a bound electron, transferring the photon momentum to the electron. If the energy of the photon is higher than the binding energy of the electron, the atom is ionised, leaving behind a core hole. σ_{ph} declines as the energy of the photon increases beyond the characteristic ionisation energies, and increases with the atomic number of the attenuating material. σ_{ph} increases discontinuously at the ionisation energies, and these discrete jumps are commonly referred to as absorption edges.

Between and beyond the absorption edges the energy dependence of the photoelectric effect is roughly estimated as

$$\sigma_{pe} = C\frac{Z^n}{E^3} \tag{3}$$

where C is a constant, Z is the atomic number of the material, E is the energy of the incoming photon and n is a number that varies between 4 and 5 depending on the energy.

Compton scattering is the process in which photons are scattered by free electrons. Electrons bound to an atom may be considered free when the energy of the incoming photon is much larger than the binding energy of the electron. σ_C is an important source of attenuation for photonenergies between 10 keV and 10 MeV range, but is less significant in heavier materials in which the photoelectric effect is stronger.

Pair production is when a photon creates an electron and a position pair which is only possible when the photon has an energy above 1.022 MeV, and will not be further discussed here.

σ_{tot} is the combination of all photon-matter interactions, and represent the total likelihood of an interaction occurring. The total attenuation in a material can be represented by a linear attenuation coefficient μ_l

$$\mu_l = \eta_a\sigma_{tot} \tag{4}$$

where η_a is the number of atoms per unit mass.

4

The attenuation depends on the energy of the incoming X-rays, and which material it passes through. The transmittance, T, of a material is related to μ_l by

$$T(E) = \frac{I_{trans}(E)}{I_0(E)} = e^{-\int_0^t \mu_l(E,z)dz} \tag{5}$$

where I_{trans} and I_0 are the transmitted and incoming intensities respectively and t is the thickness of the material along the transmission direction $\vec{z}$. $\mu_l(E,z)$ is the energy dependant linear attenuation coefficient at a point z.

The Beer-Lambert law for transmittance through multiple distinct regions is a direct result of Eq. (5):

$$\frac{I_{trans}(E)}{I_0(E)} = exp\left(-\sum_i \mu_l(E)_i t_i\right). \tag{6}$$

where t_i is the thickness of a region with a uniform attenuation coefficient $\mu_l(E)_i$.

The mass attenuation coefficient, $\frac{\mu(E)}{\rho}$, is a tabulated value which is used to calculate μ_l for materials depending on density and composition. μ_l for a compound can be calculated by applying the weight fraction ω for each element in the compound

$$\mu_l(E)_i = \rho_i \sum_j \left(\frac{\mu(E)}{\rho}\right)_j \omega_j. \tag{7}$$

where ρ_i is the density of the compound as a whole.

The linear attenuation coefficient is proportional to the density of the material, which means that high-density materials such as metals usually have a linear attenuation coefficient several orders of magnitude larger than that of a gas. In a two-phase sample the significance of the lighter material can be determined by comparing the linear attenuation coefficients by using Eq. (7). The mass attenuation coefficient for solid aluminium and air is of the same order of magnitude, and comparable in the 100 keV - 10 MeV range[5]. However the density of aluminium three orders of magnitude larger than that of air as $\rho_{Al} = 2.699 \, \mathrm{g\,cm^{-3}}$ while $\rho_{Air} = 1.205 \times 10^{-3} \, \mathrm{g\,cm^{-3}}$[5]. Taking the difference in densities into account, the attenuation in air can be considered negligible for a sample with $t_{Air} < 20 t_{Al}$, meaning an aluminium foam with an aluminium fraction of ¿5% can be approximated as a single phase sample in vacuum.

2.3. Measured intensity

X-rays are most commonly detected by indirect detectors, i.e. by conversion of the x-ray photons into another signal which is then detected. In x-ray imaging the most common indirect detectors are based on scintillator materials, which absorb x-ray photons by atomic excitation. The exited state in the scintillator decays by emitting a photon in the visible light region which is detected using conventional photosensors such as CCDs of CMOS cameras.

The detection efficiency of a scintillator detector is dependant on the amount of attenuation in the scintillator. The amount of attenuation can be found by using Eq. (6)

$$\frac{I_{Att}(E)}{I_i(E)} = 1 - \frac{I_{Trans}(E)}{I_i(E)} = 1 - e^{\mu_d t_d} \tag{8}$$

where μ_d is the linear attenuation coefficient of the detector and where I_i is the incoming intensity after any attenuation that occurs between the source and detector. Thus I_i is given in accordance with Eq. (6)

$$\frac{I_i(E)}{I_0(E)} = exp\left(\sum_k \left(\frac{\mu(E)}{\rho}\right)_k \rho_k t_k\right) \tag{9}$$

where k denotes the sources of attenuation along the beam path.

The measured intensity, I_{meas}, is the amount of x-rays that are attenuated in the detector, I_{Att} in Eq. (8).

$$I_{meas} = I_{Att} = \frac{I_{Att}}{I_i}\frac{I_i}{I_0}I_0 \tag{10}$$

where I_i is given by Eqs. (7) and (9), and I_0 is energy dependant as per Eqs. (1) and (2). Thus

$$I_{meas}(\overrightarrow{r}) = \int_0^{E_{max}} I_0(E)exp\left(\sum_k \mu_k(E, \overrightarrow{r})t_k(\overrightarrow{r})\right)(1 - exp(\mu_d(E)t_d))dE. \tag{11}$$

where $\overrightarrow{r}$ signifies the beam path.

2.4. Calculating total thickness

The total thickness of a sample with a known μ_l can be calculated from I_{meas} by placing the sample in an environment with no additional in-homogeneous sources of attenuation. $I_0(E)$ can be determined by Eqs. (1) and (2) if the source-specific constants k_1 and k_2 are known. μ_d of the detector can be calculated according to Eq. (7), while t_d is a known property of the detector. Any additional sources of attenuation, such as air or detector housing, is independent of the beam path. I_{meas} can thus be calculated according to Eq. (11) as a function of t_s. The total thickness of the material along the beam path may then be determined based on the measured intensity.

2.5. Radiography and Computed Tomography

Radiography is conducted by placing a sample between an x-ray source and an x-ray detector such that the x-ray beam passes through the sample and the transmitted x-rays are recorded by a detector. The detector is segmented into smaller pieces, pixels, which individually measure the incoming intensity. For each pixel in the detector the intensity observed is

given by Eq. (11), with each pixel measuring the intensity which passes through a different beam path in the sample. The beam path for each pixel is different, causing the amount of attenuating material along the beam path to vary. The difference in attenuation along the beam paths causes the pixels in the detector to receive a different amount of incoming radiation. The image recorded by the detector will be an intensity image that shows the attenuation contrast in the sample.

For a parallel beam, the resolution in the sample is given by the physical spacing of the pixels in the detector, A_{pixel}. For a conical beam, such as the one generated by a point source, the sample will be subject to a geometric magnification, and the resolution will increase accordingly. The geometric magnification factor G of the sample is determined by the distance between the source and sample, SOD, and the distance between the source and detector, SDD:

$$G = \frac{SDD}{SOD} \tag{12}$$

The effective pixel size is $\frac{A_{pixel}}{G}$, which is the resolution of the sample.

By backprojecting the radiograms from multiple different angles it is possible to reconstruct the sample in three dimensions. This reconstructed object is commonly referred to as a computed tomogram, or CT. The resolution of the tomogram depends on the effective pixel size of each radiogram and the number of different projections among other factors.

2.6. Correlating position

Let us define y as the direction from the source to the detector, x as the horizontal orthogonal to y and z as the vertical orthogonal to y and x. (x=0, y=0, z=0) is the point along the y-axis that is halfway through the sample. u and v are the position in the detector, with u parallel to x and v parallel to z. For a conical beam the x-ray beam which goes through a point (x,y,z) in the sample will hit the detector in a point (u,v) determined by Eqs. (13) and (14)

$$u(x, y) = \frac{x}{SOD + y} \cdot SDD \tag{13}$$

$$v(y, z) = \frac{z}{SOD + y} \cdot SDD \tag{14}$$

where SOD is the distance between the source and the sample and SDD is the distance between the source and detector, see Fig. 2.

2.6.1. Stereo Vision

A stereoscopic image of the sample can be obtained by shifting the sample a distance x_s to one side and record a second radiogram. The stereoscopic image can be used to determine the depth of a feature in the sample. From Eq. (13) the shift u_s of a feature in the projection is

$$u_s = \frac{x_s}{SOD + y} \cdot SDD. \tag{15}$$

As u_s in only dependant on y for a known x_s it is possible to determine the y position of a feature in the sample by measuring u_s

$$y = \frac{SDD}{u_s} \cdot x_s - SOD. \tag{16}$$

If there exist a reference point at $y = 0$ with the shift u_{ref}, y can be calculated as

$$y = \left(\frac{u_{ref}}{u_s} - 1 \right) SOD \tag{17}$$
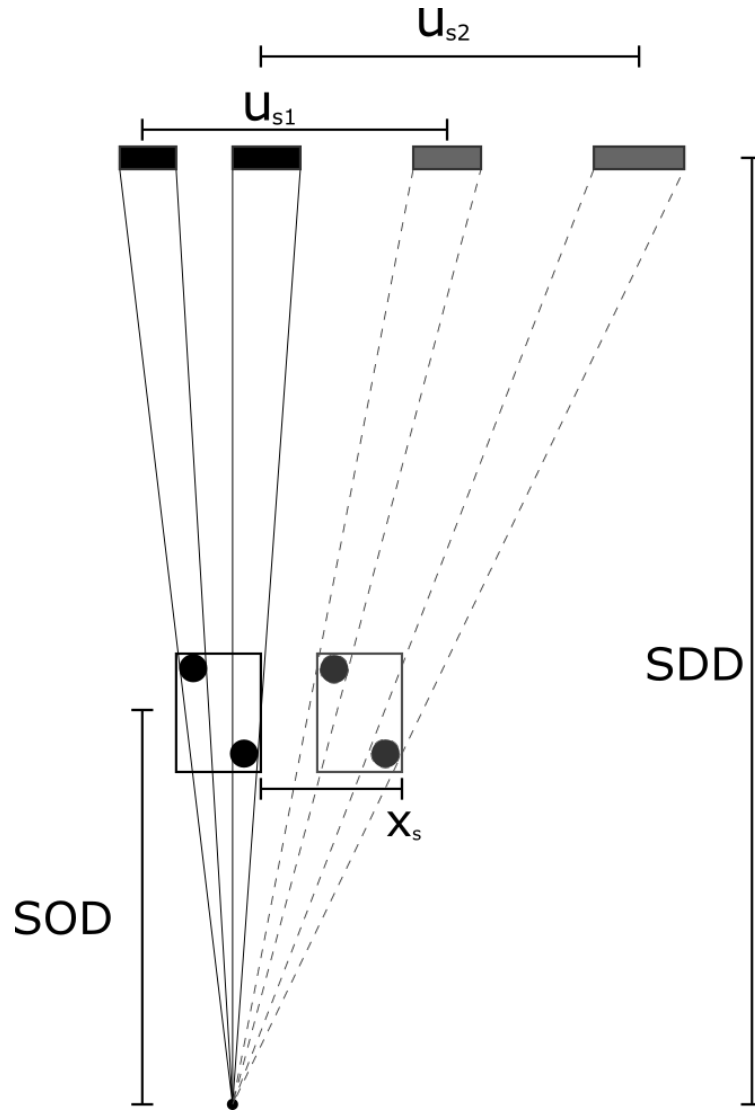
2.7. Basics of mechanical deformation

Figure 2: A sample with two features is projected into a detector by a cone beam. As the sample is shifted x_s to one side, the two features is shifted a different distance in the projection, depending on the y-position of the feature within the sample. A feature far from the source is shifted a distance u_{s1}, which is smaller than the shift of a feature close to the source, u_{s2}.

3. Experimental

3.1. Metal foam sample production

The sample in this experiment was produced by the "powder compact melting technique", often called "powder metallurgical", which consist of mixing a powder of the desired metal with a "blowing agent", a compound which releases a gas when heated. After being mixed together two powders are pressed into a compact block before being heated. Upon heating the mixture the blowing agent start releasing gas into the metal such that the gas form cavities. The powder metallurgical technique results in well distributed pores, with a solid surface layer. For aluminium compounds, TiH_2 is often used as a blowing agent.[2]

3.2. Setup

For this experiment a $25\,mm \times 25\,mm \times 15\,mm$ piece of aluminium foam was cut from the interior of a larger section. The regions which lie close to the surface of the metal foam during production have a much higher density than the interior, and the surface regions can not be considered representative for the material behaviour. For the metal foam used in this experiment the total height of the produced foam was $90.5\,mm$ and the region with significantly higher density was $13\,mm$ on the top and bottom. The sample was cut from the interior of the sample to avoid any effects from the high density regions near the surfaces. The sample was placed in a Deben compression rig, with $2\,mm$ thick PVC discs above and below to separate the sample from the compression plates. The separation was done to be able to distinguish between the sample and compression plates and to minimise interference from the highly attenuating compression plates. The compression rig consisted of two steel compression plates connected by a carbon-glass tube. The tube was homogeneous for all angles and rotated with the sample. The attenuation of the tube was 25% of the x-rays.

The experiment was conducted on a Nikon XT H 225 ST at the Institute of Physics at NTNU. The x-ray generation was done in a sealed tube generator with a Wolfram target, an acceleration voltage of $170\,kV$ and a beam current of $135\,\mu A$. The detector was a PE 1620 sensor with a $550\,\mu m$ Caesium Iodine scintillator. The compression rig with the sample was placed $12\,cm$ from the x-ray source, while the detector was mounted $112\,cm$ from the X-ray source. An illustration of the setup can be seen in Fig. 3. The exposure time for each projection was set to $1000\,ms$, and the gain was set to $18\,dB$.

3.3. Compression

The compression of the sample was done in a series of steps that was $200\,\mu m$ to $500\,\mu m$ per step. Radiograms were recorded along the x-axis and y-axis of the sample, each radiogram being the average over 16 consecutive exposures to average random errors. In addition to this a set of radiograms were collected along the x-axis with the sample shifted 5 mm along the y axis.

Each step were controlled by fixing the travel distance of the compression plates to ensure a high degree of control during the experiment, and the possibility of pausing the compression
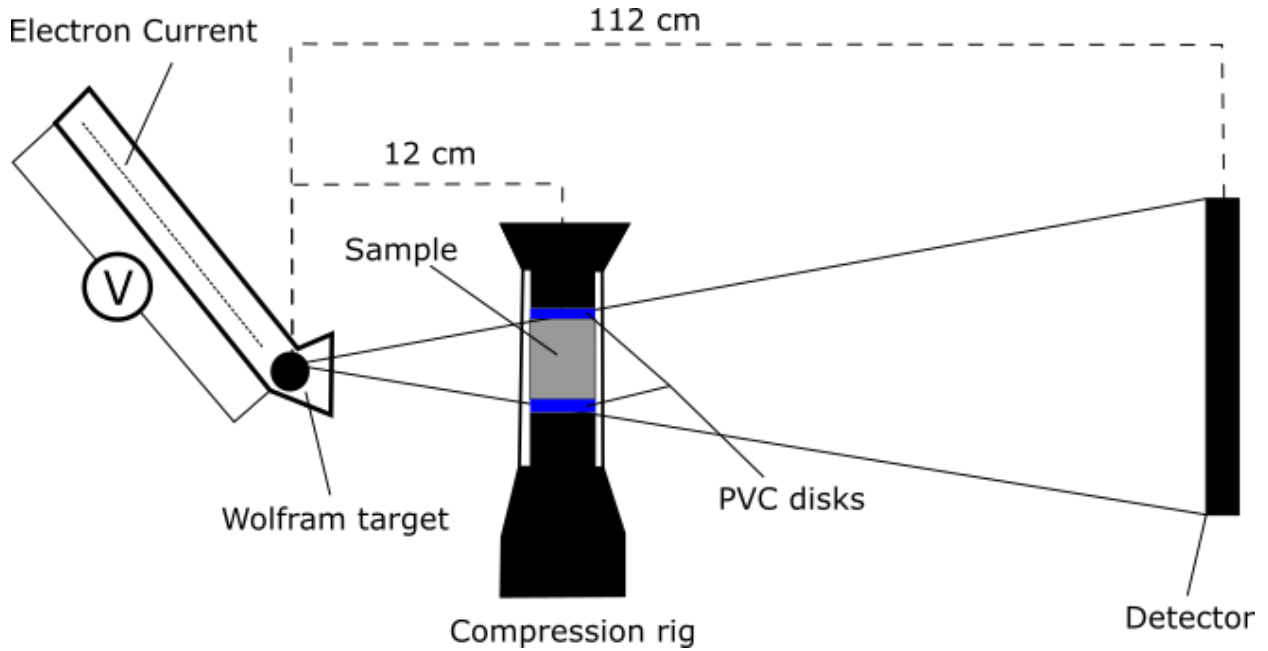
Figure 3: A schematic for the setup of the experiment. The compression rig with the sample is placed between the source and the detector 12 cm from the x-ray source. The sample have been separated from the compression plates by two 2mm thick PVC discs.

to examine the radiograms for any significant changes. The stress-strain curve was monitored closely during the compression to determine when to perform intermediary tomograms. Two tomograms were taken during elastic deformation, one tomogram near the yield point of 5.2% strain and then regular tomograms until the sample had been compressed by 20%. The list of tomograms can be seen in Table 1.

3.4. Source characteristics

To identify the source specific constants necessary to calculate the produced energy spectrum, an experiment have previously been conducted on a similar setup by Nikon, which can be assumed to apply to the source used in this experiment as well. The experiment conducted by Nikon used an energy dispersive detector to measure the full energy spectrum from two different acceleration voltages. All sources of attenuation in this setup was known, and the only unknown quantities in Eqs. (1), (2) and (11) were the source specific constants k_1 and k_2. Initial energy spectra for both voltages was generated using an arbitrarily chosen k_1 and k_2 and Eq. (1), which was then used in Eq. (11) to obtain the final energy spectra. The two final energy spectra was compared to the two measured energy spectra, and k_1 and k_2 were changed to reduce the difference between the calculated and measured energy spectra. Using an optimisation algorithm, values for k_1 and k_2 were determined to be 0.03625209 and 0.01151299 respectively for the type of source used in this experiment.

The x-ray spectrum generated from the source used in this experiment can be calculated by Eqs. (1) and (2). The characteristic X-ray energies of Wolfram are retrieved from a table

11

Table 1: The compression process was stopped at selected points to perform full tomographies of the sample. The yield point of the sample was located at 5.2% strain. The aluminium fractions were calculated from the tomograms

Compression [mm]	Strain [%]	Aluminium Fraction [%]
0	0	9.04
0.20	1.33	8.90
0.40	2.67	9.17
0.78	5.2	9.08
1.00	6.67	9.33
1.50	10	9.59
2.25	15	10.52
3.00	20	10.30

published by the National Physics Laboratory, UK[6]. The detected spectrum with the setup attenuation is given by Eq. (8).
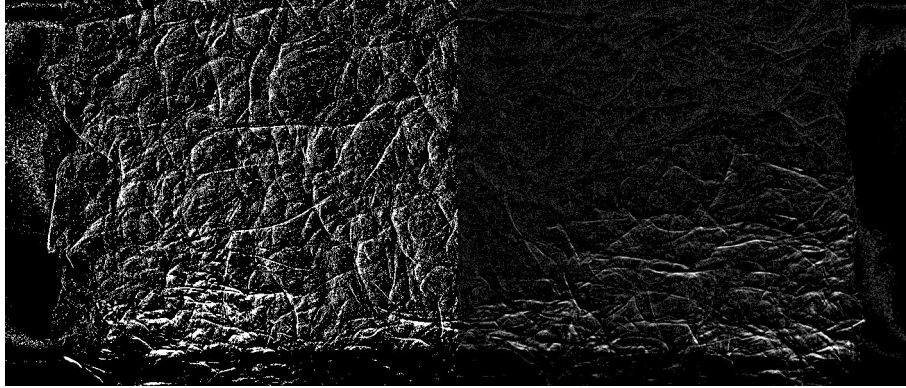
Figure 4: Left side shows the direct difference image at 5% compression, while the right side shows the difference image corrected for the overall shift.

4. Results

4.1. Adjustments and calculations

This section will present the calculations and adjustments done in order to characterise the sample and extract the relevant data from the radiograms and tomograms.

4.1.1. Pore fraction

To determine the pore fraction of the sample a threshold was applied to each slice of the tomogram, assigning each pixel as either air or aluminium. The aluminium fraction of the sample was determined as the percentage of pixels designated as aluminium. The aluminium fraction of the sample for each tomogram is shown in Table 1.

4.1.2. Image correlation corrections

When aluminium foam undergoes plastic deformation some pores collapse while others remain intact. Large regions of intact pores may be considered as a semi-static region which maintains its internal structure. As pores in surrounding regions collapse however, the semi-static regions are translated in relation to the setup. A direct difference image between two projections will show a large amount of change in the semi-static regions due to this translation. When identifying deformations the translation of semi-static regions is uninteresting, and it is desirable to reduce the translation signal in the difference images to better detect deformations.

A semi-static region was selected as a reference region for the difference images. Each image was translated such that the reference regions in each projection were as close to identical as possible. The same translation was then applied to the full projection, causing the translation signal for that semi-static region to be minimised while still keeping the deformation signal. The translation corrections greatly reduced the noise in the static region, and the effect on the difference image can be seen in Fig. 4.
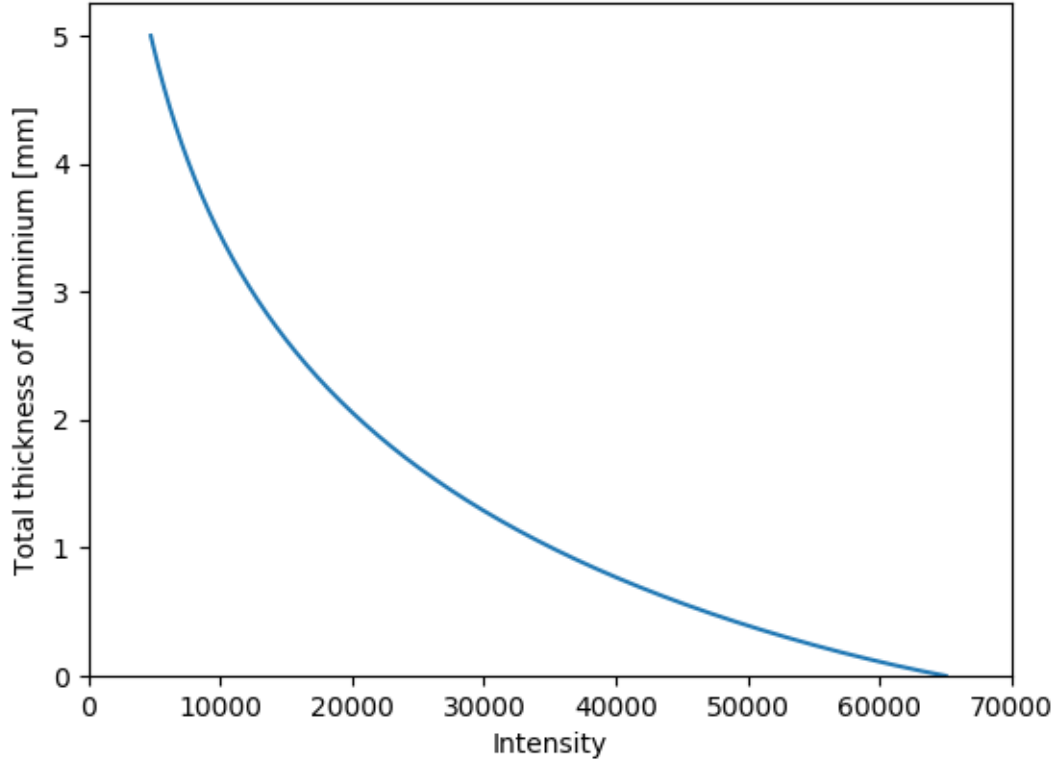
Figure 5: Density as a function of intensity. Determined as the inverse of $I_{meas}(t)$, which is calculated by Eq. (11)

4.1.3. Thickness calculation

For a known source passing through a single-phase sample the measured intensity can be expressed as a function of total sample thickness. The measured intensity is calculated according to Eq. (11) for different sample thicknesses. The inverse of $I_{meas}(t)$, shown in Fig. 5, can be used to determine the thickness from the radiograms.

4.1.4. Identification of a pore

When a change was detected in the difference image of the radiograms, the tomograms before and after the deformation were analysed in the region of interest to determine the source of the deformation signal. Features that had changed from one tomogram to another were determined to be the same based on being in the position and having similar surrounding regions. This was done manually as the deformations made identification by software difficult.

14

4.2. Wall buckling

This section will examine the changes observed in an aluminium wall from 2.67% compression, the location of which is shown in Fig. 6a. The deformation was first detected after 3.3% compression in the radiogram difference images, as seen in Fig. 6b, and consist of an aluminium wall buckling and then breaking.

The deformation was first detected in the radiograms after 3.3% compression, Fig. 6b, and determined to start after 2.67%. Until 10% compression the wall is the only deformation event in the local region, and is clearly identifiable in the difference images. After 10% compression some of the immediately surrounding region in the projection is also deformed, but the wall is still identifiable both in the radiogram and the tomograms. By examining the tomograms at 2.67% and 5.2% compression, Figs. 8a and 8b, the aluminium wall can be seen to go from no deformation to a buckled wall. The angle formed by the wall in each tomogram was compared to the respective radiogram, see Figs. 7a and 8b. At 5.2% compression the angle of the wall was found to be X±Y°in the radiogram and X±Y°in the tomogram. The radiograms show a sharp angle in the wall at 10% compression, Fig. 7b, which corresponds with the angle in the 10% compression tomogram, Fig. 8c.

4.3. Pore collapse between static regions

This section will examine the changes observed in a pore located between two mostly static regions. The radiograms show that the deformation occurred after 8% compression, see Figs. 9 and 10.

A pore was found in the 6.7% compression tomogram which corresponded with the shape seen in the density image at the same level of compression, see Figs. 11a and 12a. The 10% compression tomogram show that the pore have been deformed in a way which corresponds well with the radiogram, see Figs. 11b and 12b. The pore was identified as the same pore based on its recognisable shape, its location within the sample and having a matching surrounding region, specifically the junction under the pore and the two parallel walls above the pore.

4.4. Event in the surface region

A deformation was detected around 12% compression near the bottom of the sample, the location of the pore can be seen in Fig. 13. A horizontal pore wall was observed bending as one side of the wall was rising while the other remained stationary, see Fig. 14d

When examining the 10% tomogram to identify the structure prior to deformation, it became apparent that the pore was already partially compressed, see Fig. 14c. Examining the pore in all tomograms, the 6.67% tomogram show a broken wall at the bottom of the pore where for earlier tomograms this wall was whole, see Fig. 14b

Upon closer inspection the radiogram showed a deformation in the region which was initially overlooked. This was due to the decreased contrast between the aluminium and background in the radiogram as the x-ray beam travelled through both the sample and the PVC disks
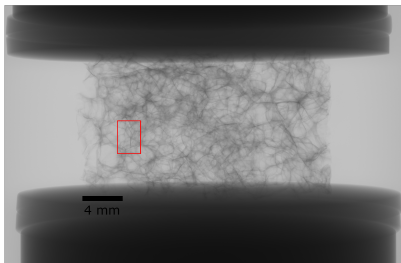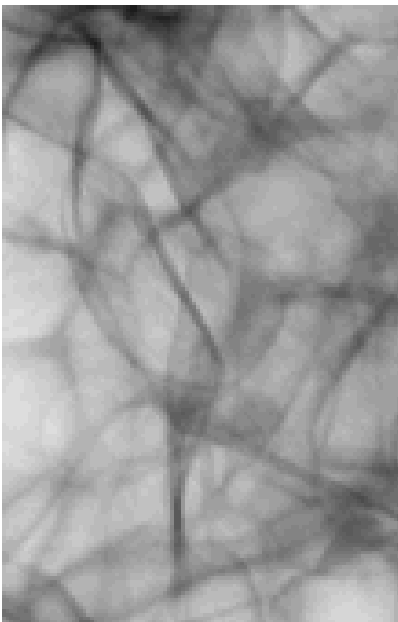
(a) The location in which a deformation was seen is shown in red.
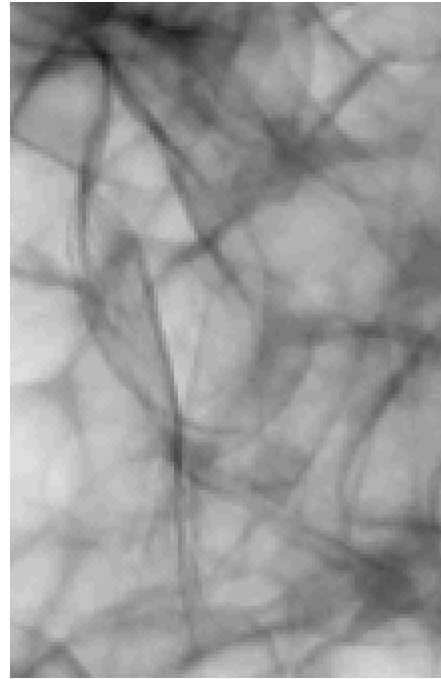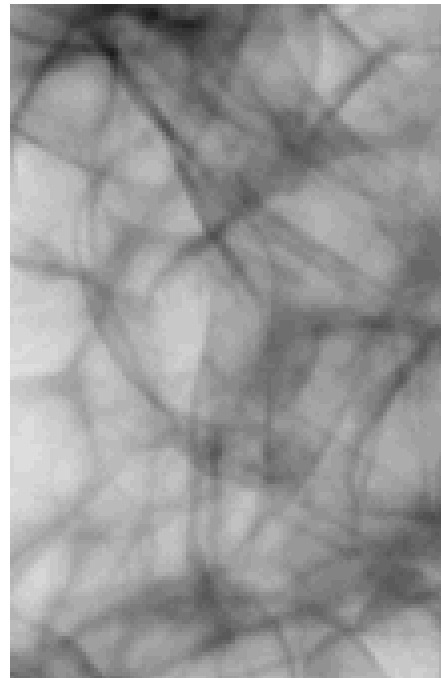

(b) The difference between the radiograms at 3.3% and 3.7% compression. The lighter area shows a difference in density between the two radiograms due to a deformation of an aluminium wall.

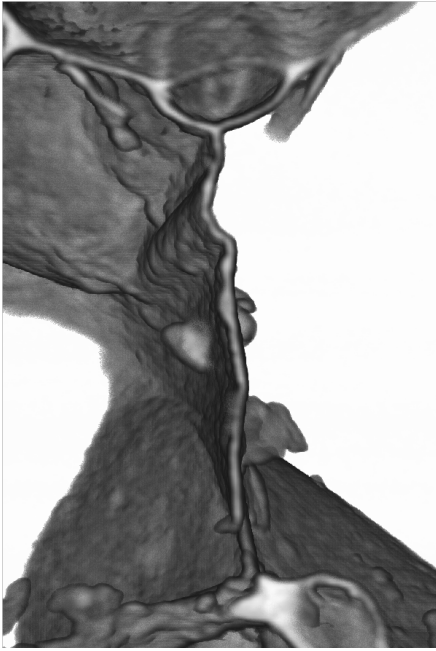Figure 6: A deformation was detected after 3.3% compression in the area highlighted in (a).

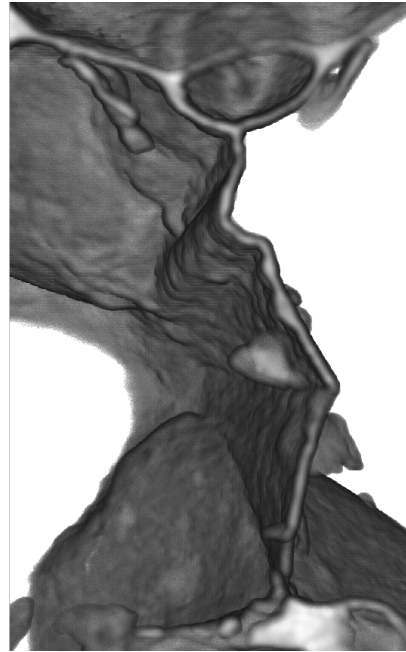(a) The density image at 5.2% compression shows that the shape forms a 138°angle.
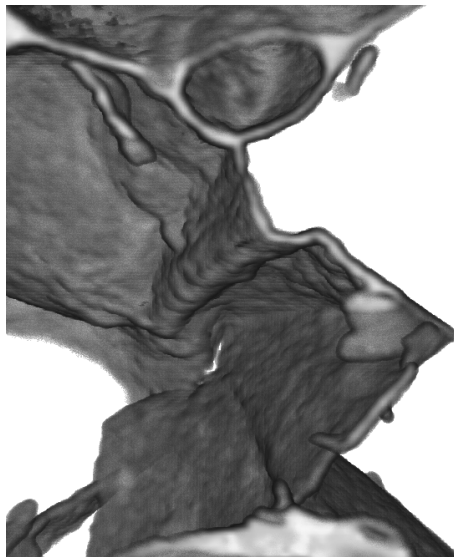

(b) After 10% compression the deforming shape now forms a 83°angle

Figure 7: The density image in the region shown in Fig. 6a at 5.2% and 10% compression

(a) The aluminium wall after 2.67% compression. The wall is mostly straight and show no signs of deformation.

(b) After 5.2% compression the wall is bent such that it forms a 138°angle

(c) After 10% compression the wall forms a 83°angle.

Figure 8: An aluminium wall in the sample, depicted along the y direction after (a) 2.67%, (b) 5.2% and (c) 10% compression. The surrounding region was used as a reference to get images of the wall from the same point of view.
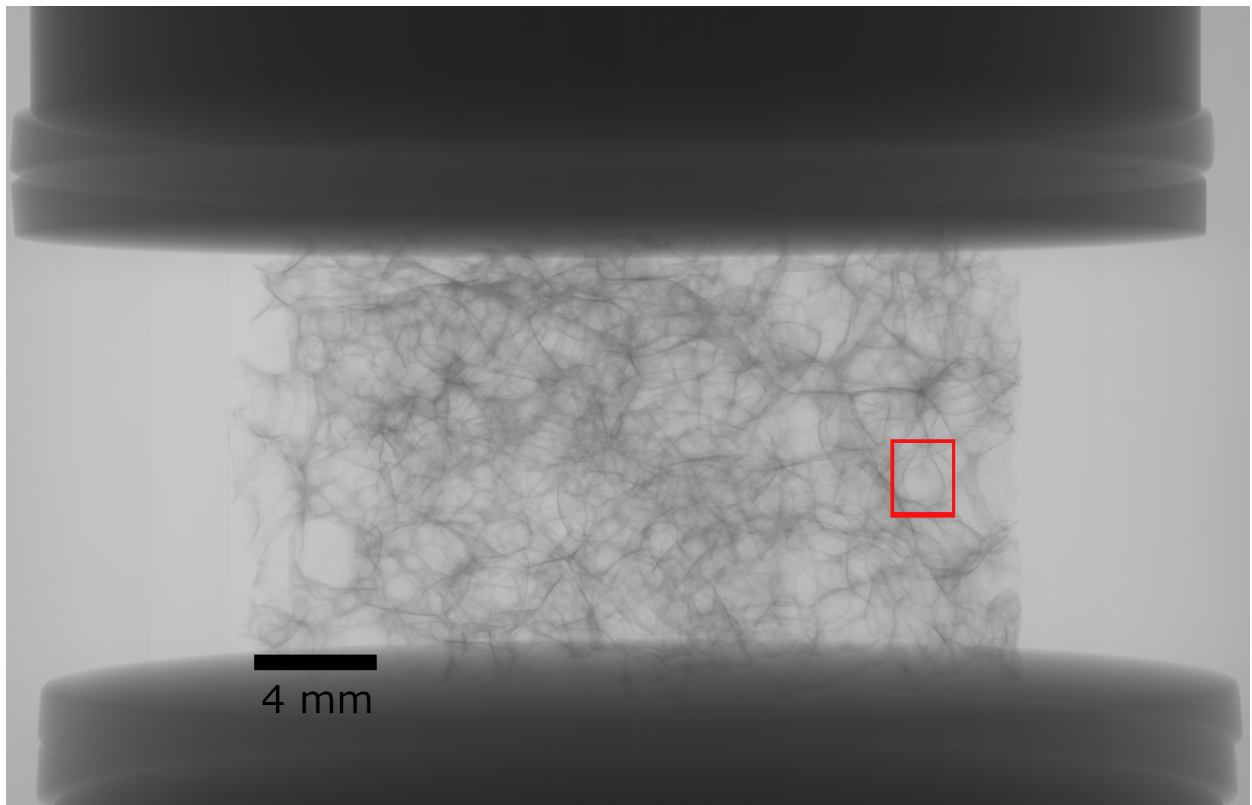
Figure 9: A pore with a distinct shape which deformed during the compression was observed here
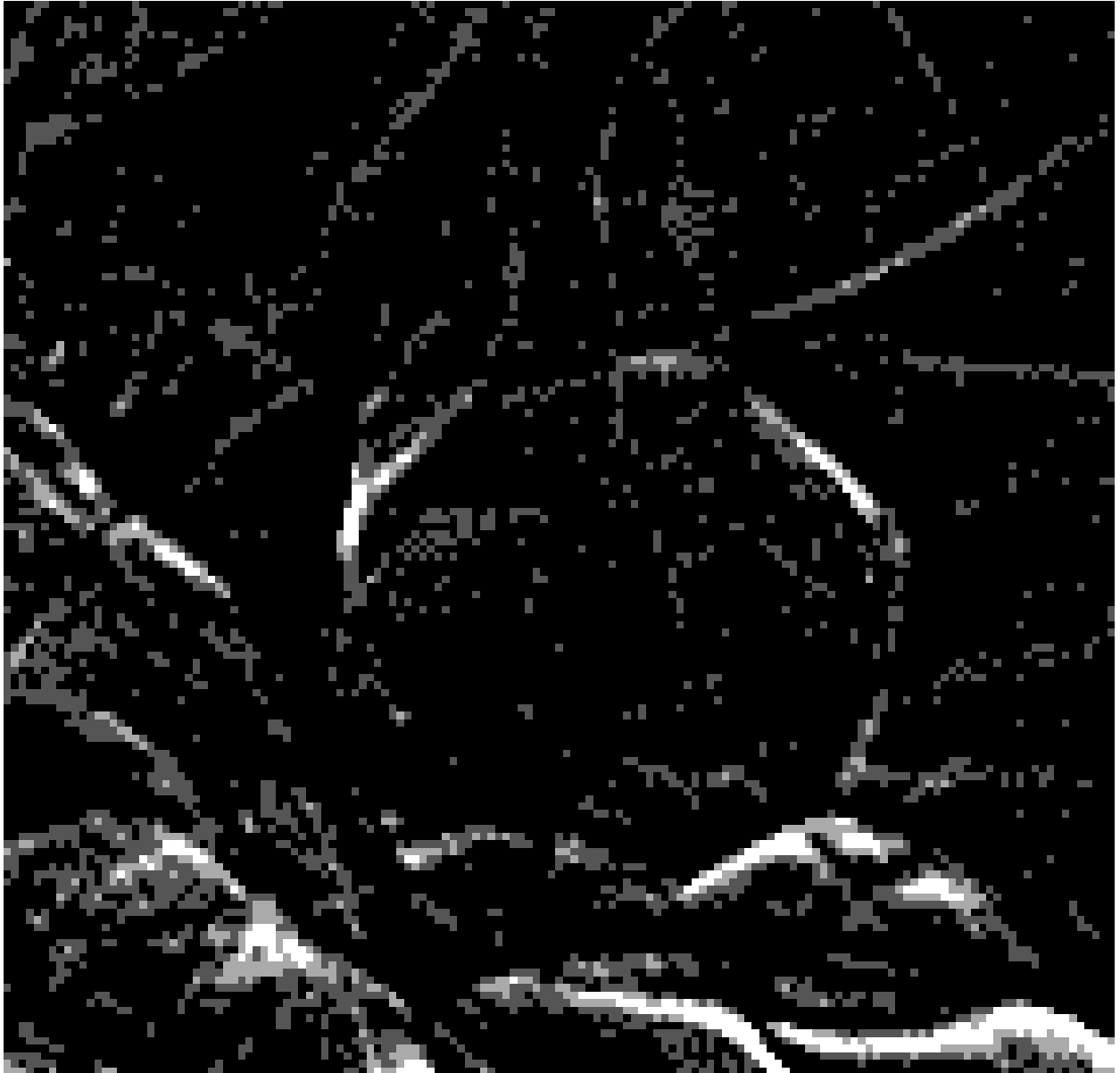
Figure 10: A pore with a distinct shape which deformed during the compression was observed here
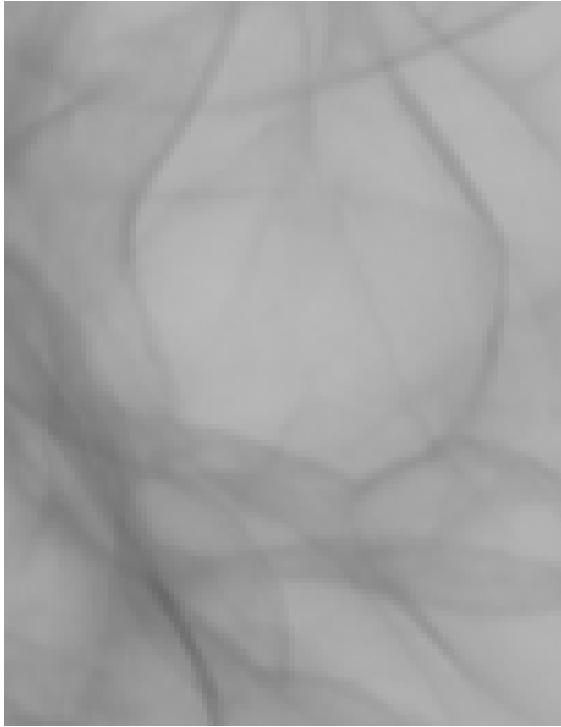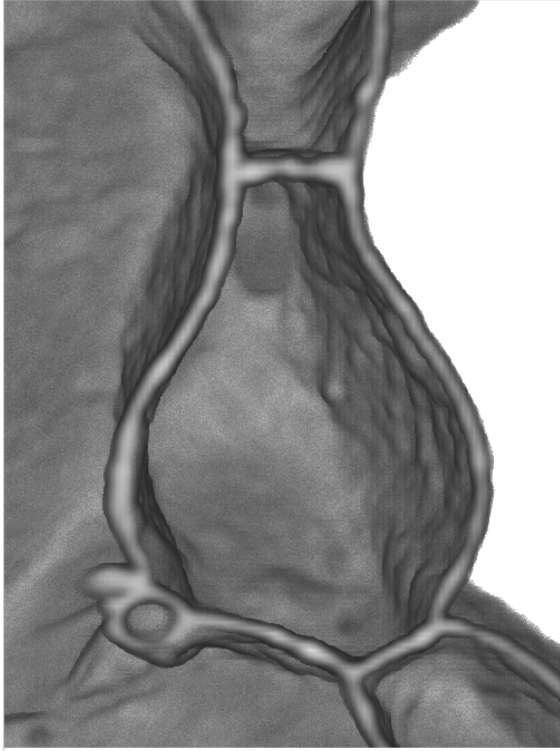
(a) The density image at 6.67%   (b) The density image at 10%
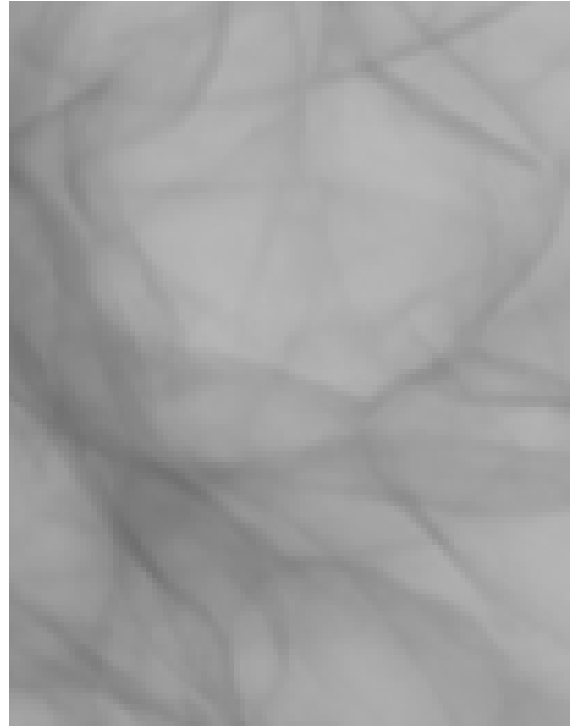
Figure 11: Density image of the region shown in Fig. 9 at 6.67% and 10% compression.

placed below the sample. A deformation was identified starting at 3.67% compression, with the wall breaking at 5.9% compression. The intial pore can be seen in Fig. 14a.

(a) The pore at 6.7% compression. The distinct shape implies that this pore is the origin of the shape observed in Fig. 11a
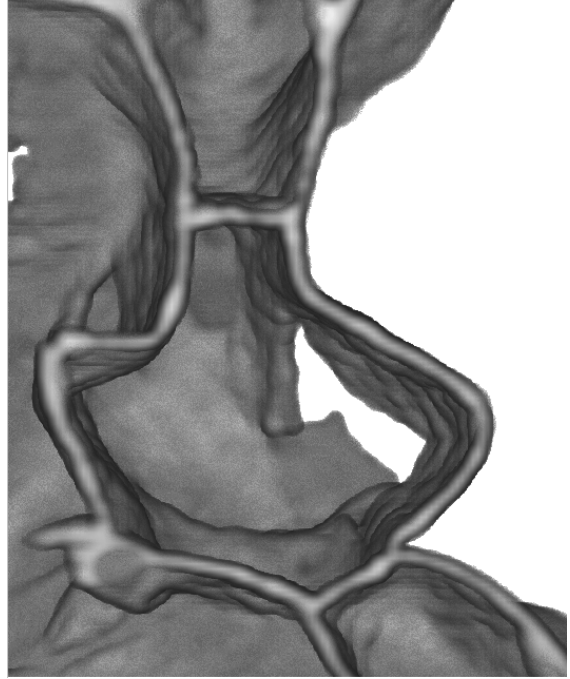
(b) The same pore as shown in (a), from the 10% tomogram. The pore has been deformed and a rift in the pore back wall is visible. The wall of this deformed pore match the shape in Fig. 11b.

Figure 12: A pore at 6.7% and 10% compression, seen along the y-axis of the sample. The pore show clear deformation during the compression, causing the signal in Fig. 10.

5. Discussion

The tomograms and radiograms show a clear similarity between the shape of a pore or pore wall in the sample and the shapes in the attenuation contrast in the radiogram. As the sample is compressed the structure in the tomogram changes, and the shape in the radiogram change in the same fashion. This is true for all the events examined as part of this thesis, and it stand to reason that it will be true for all similar events. It is worth noting that the events identified were of walls parallel to the projection direction. This is likely due to the increased amount of attenuation in a parallel wall compared to a transversal wall. Any deformation in such a wall represent a large shift in the attenuation for two adjacent beampaths, which is very visible in the difference images. Thus changes in the sample which may be observed in a tomogram may not be observable in a given radiogram.

When using stereoscopic imaging to determine the position of a feature, the position calculated by Eq. (17) diverged from the position determined by examination of the tomogram by up to 15% of the sample thickness. The uncertainty in calculated position is largely dependant on the uncertainty of the sample position, SOD, which for this experiment has
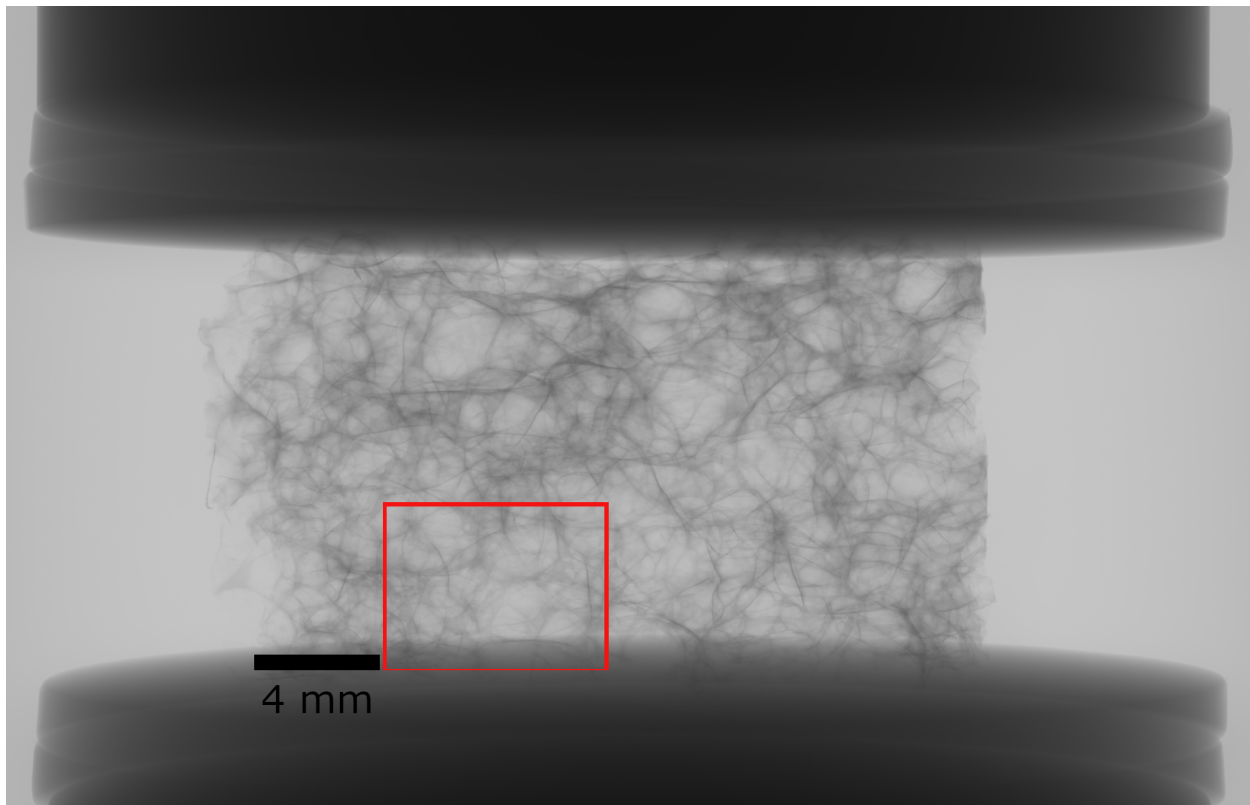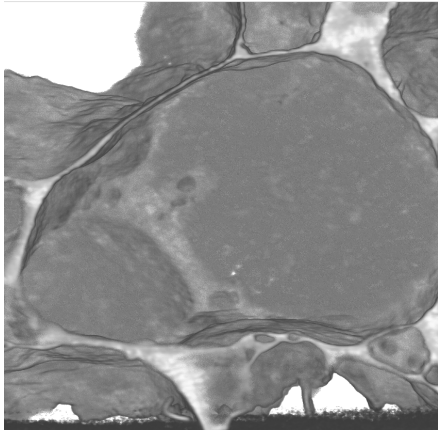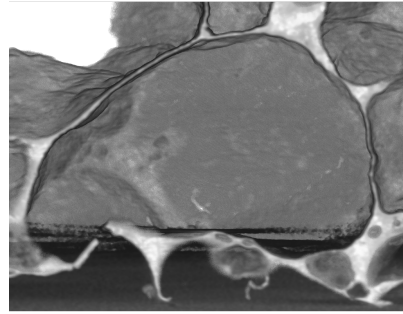
Figure 13: A pore near the surface which was deformed in two stages. The first stage was not detected initially from the radiograms due to the increased background attenuation from the PVC disks.
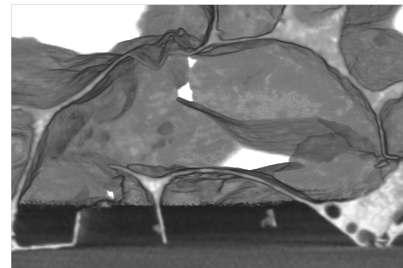
(a) The initial pore before any compression

(b) After 6.67% compression the bottom of the pore have a broken wall. This deformation was more difficult to detect due to the increased background attenuation in the radiogram.
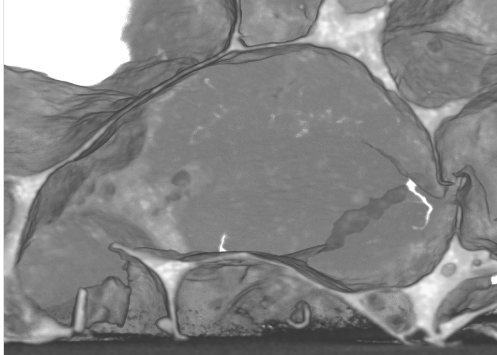
(c) After 10% compression the bottom of the pore has collapsed, but the top of the pore is still intact

(d) After

Figure 14: A pore located near the bottom of the sample. The tomogram show that the pore was deformed at two different times.

an uncertainty of 5%. As the calculated position deviate much more from the measured position than the expected uncertainty, the calculated position must be subject to another error, possibly in the reference shift, or a larger error than expected in the sample position. The source of this error was not determined for this experiment and as such the calculated positions based on stereoscopic imaging can not be considered true. A relative shift between features in the radiogram can still be considered an effect of the two features being a different distance from the source however, and can as such be used to determine that two features in the radiogram are not immediate neighbours in the sample.

6. Conclusion

In situ radiograms showing deformation were compared to the tomograms acquired before and after the deformation to determine whether the changes observed in the radiograms were the projections of specific events in the tomograms. Several events were detected in each of the radiograms which were then examined in the tomograms taken during the compression process. The structures observed in the radiogram were identifiable in the tomogram by comparing angles within the features and their orientation in the sample. The same structure was identified in each tomogram and compared to the projection in the tomogram, and in each case the shape of the projection matched the shape of the feature. The uncertainty in the angles in the tomograms and radiograms was less than [X]%, and the identical angles in the tomograms and radiograms thus confirms that these were the result of the same structure. The size of the feature was subject to a 20% uncertainty in the radiogram due to the geometric magnification and the thickness of the sample, and was as such not used to identify features as the same.

Every clear feature observed in the radiograms proved to be the result of a deformation in a wall parallel to the projection direction as it represented a larger change of attenuation than a deformation in a transverse wall. Future in situ work with this technique will have to consider the need for time-resolution to determine the optimal number of projection directions, as each projection direction will increase the number of events detected, but decrease the time-resolution of the in situ radiograms.

The possibility of using stereoscopic imaging to determine the position of features in the sample were explored, but the positions calculated by this technique diverged by up to 15% from the measured positions. Without a certain reference point and precise knowledge of the sample position the calculated position of a feature simply had too large an uncertainty for stereoscopic imaging to be used effectively. It can however be used to differentiate between features in the radiogram, as the relative difference in shift between two features showed that they were not in the same transverse plane.

References

[1] J. Banhart and J. Baumeister, "Deformation characteristics of metal foams," *Journal of Materials Science*, vol. 33, pp. 1431–1440, 1998.

[2] J. Banhart, "Manufacture, characterisation and application of cellular metals and metal foams," *Progress in Materials Science*, vol. 46, pp. 559–632, 2001.

[3] H. A. Kramers, "On the theory of x-ray absorption and the continuous x-ray spectrum," in *Collected Scientific Papers*, pp. 134–155, Amsterdam: North-Holland Publishing company, 1956.

[4] H. L. Monaco, "Experimental methods in x-ray crystallography," in *Fundamentals of Crystallography* (C. Giacovazzo, ed.), ch. 4, pp. 229–318, Oxford: Oxford University Press, 1992.

[5] J. H. Hubbell and S. M. Seltzer, "Nist standard reference database 126: X-ray mass attenuation coefficients." https://www.nist.gov/pml/x-ray-mass-attenuation-coefficients, 2004.

[6] D. M. Poole, "Kaye & laby, tables of physical and chemical constants: 4.2.1 x-ray absorption edges, characteristic x-ray lines and fluorescence yields." http://www.kayelaby.npl.co.uk/atomic_and_nuclear_physics/4_2/4_2_1.html.